ACS APPLIED NANO MATERIALS

Article

Cite This: ACS Appl. Nano Mater. 2019, 2, 6690−6700

www.acsanm.org

Incorporating Aluminum Plasmonic Nanohemisphere Arrays into Organic Ultraviolet Photodetectors for Improved Photoresponse

Monica R. Esopi and Qiuming Yu*

Department of Chemical Engineering, University of Washington, Seattle, Washington 98195, United States

Supporting Information

ABSTRACT: Aluminum nanostructures, which support surface plasmon resonances in the UV spectral range, were incorporated into conventional organic UV photodetectors with a structure of indium tin oxide (ITO)/poly(3,4-ethylenedioxythiophene):poly(styrenesulfonate) (PEDOT:PSS)/poly(9,9-dioctylfluorene-*alt*-bithiophene) (F8T2):[6,6]-phenyl-C_{71}-butyric acid methyl ester ($PC_{71}BM$)/LiF/Al. Nanohemisphere arrays (NHSAs) were imprinted into the top surface of the soft organic active layer, thus transferring the pattern to the subsequently thermally deposited layers of LiF and Al. NHSA-top devices and flat-top control devices were investigated by 3-dimensional finite-difference time-domain (3D-FDTD) electromagnetic simulations. Improved UV active layer absorbance and enhanced electric fields in the nanohemispheric region at the top of the active layer were shown for devices with the NHSA-top. The impact of the NHSA-top was found to be more significant for devices with thin active layers and to gradually decrease with increasing active layer thickness. Fabricated NHSA-top devices with thin active layers exhibited improved photoresponse in terms of external quantum efficiency, specific detectivity and on−off response speed compared to flat-top devices under 330 nm illumination and 0 to −1 V bias. The method developed in this work provides a versatile and effective way to incorporate plasmonic nanostructures into optoelectronic devices to enhance device performance.

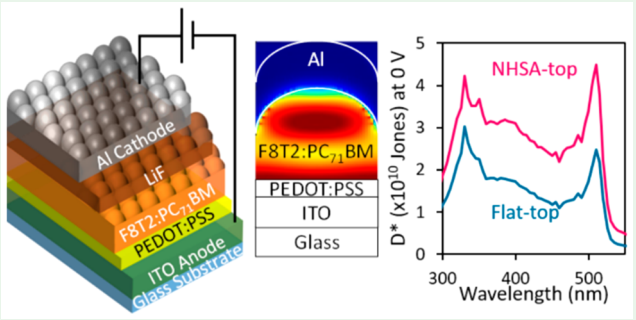

KEYWORDS: *aluminum plasmonic nanostructures, enhanced photoresponse, organic photodetectors, ultraviolet photodetectors, nanoimprinting*

INTRODUCTION

Incorporating plasmonic nanostructures at the active layer interfaces is a popular approach to improve the performance of optoelectronic devices because of performance-enhancing surface plasmon polaritons (SPPs) that are generated at metal−dielectric interfaces under illumination.[1,2] Nanostructures can be incorporated at the light-incident surface or at the rear surface of the active layer to utilize scattering and reflection of light in the active layer and enhanced local electric fields near the active layer-metal electrode interface.[2−6] The rear surface of the active layer, corresponding to the top of the film in a vertical photodiode architecture, is of particular interest for nanostructure incorporation since the nanostructures can be transferred to the top metal electrode, providing two main advantages. First, the nanostructured top metal electrode can increase the light path through the active layer due to angular reflection, thus improving light absorption in the active layer.[3,5] Second, the enhanced local electric field can positively affect light absorption and charge generation, separation and transport in the rear portion of the active layer.[5,7] It has been previously reported that light absorption at the top of the active layer dominates the spectral photoresponse produced by conventional organic photodiode photodetectors,[8−10] so nanostructures incorporated in the rear surface of the active layer could be an effective way to improve device performance. This method for enhancing photoresponse is also being actively pursued in photodetectors based on perovskite active layers, in addition to organic devices.[11]

Inspired by the structure of insect eyes and designed for green light detection, a multipattern nanostructure array consisting of nanoposts (64 nm average diameter) on a larger grating pattern (273 nm pitch) was incorporated into the top surface of an active layer composed of poly(3-hexylthiophene-2,5-diyl) (P3HT) and [6,6]-phenyl-C_{71}-butyric acid methyl ester ($PC_{71}BM$), which was included in a conventional vertical photodiode photodetector with a flexible device structure of polyethylene naphthalate (PEN)/ITO/poly(3,4-ethylenedioxythiophene):poly(styrenesulfonate) (PEDOT:PSS)/P3HT:$PC_{71}BM$ (1:1, w:w)/Al.[12] The performance of the patterned devices was compared to that of nonpatterned devices, and under 1 V bias and 532 nm illumination multipatterned devices exhibited a responsivity (R) of 7.95 A/W and a specific detectivity (D^*) of 11.4×10^{12} jones,

Received: August 18, 2019
Accepted: September 26, 2019
Published: September 26, 2019

DOI: 10.1021/acsanm.9b01586
ACS Appl. Nano Mater. 2019, 2, 6690−6700

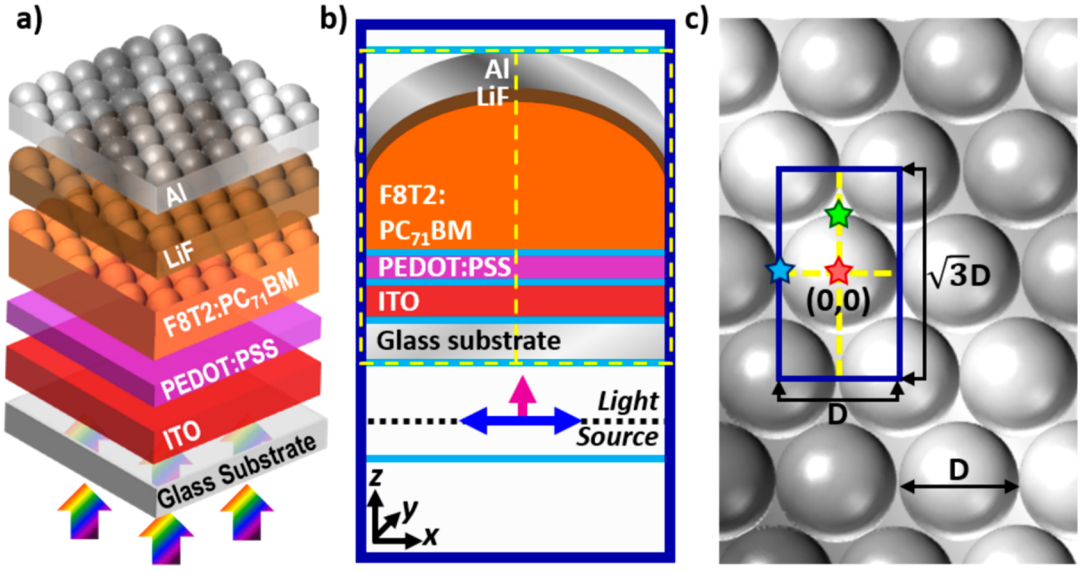

Figure 1. (a) 3D schematic of the device structure with NHSA incorporated into the active layer and subsequent layers. (b) Cross-sectional view of a simulation unit cell for a sample NHSA-top device. (c) Top-view schematic of an NHSA-top electrode showing the unit cell, the origin and the locations for vertical frequency-domain field monitors.

compared to R and D^* values of 1.48 A/W and 1.6×10^{12} jones achieved by nonpatterned devices.[12] The superior performance was arrtibuted to enhanced light trapping and absorption enabled by the multiple scaled nanostructures. Similarly, plasmonic nanostructures have been incorporated into the top active layer surface of solar cells to decrease reflection and improve light absorption, and therefore increase charge generation and photocurrent production. A 2-D square array was imprinted into the top surface of a soft polymer active layer, composed of poly[[4,8-bis[(2-ethylhexyl)oxy]-benzo[1,2-*b*:4,5-*b*′]dithiophene-2,6-diyl][3-fluoro-2-[(2-ethylhexyl)carbonyl]thieno[3,4-*b*]thiophenediyl]] (PTB7):$PC_{71}BM$, so that the pattern transferred to the MoO_3 hole transport layer and Ag top electrode in inverted organic solar cells.[13] The power conversion efficiency (PCE) was increased from 6.94% for the planar control devices to 7.74% for the devices with the plasmonic nanostructured tops due to enhancements to the short-circuit current density (J_{SC}). A nanohemisphere array (NHSA) was imprinted into the top active layer surface of quantum dot (QD) solar cells with a structure of ITO/ZnO/PbI_2-QD/PbS-QD/Au, so the pattern transferred to the top Au electrode.[14] Patterned devices produced an average J_{SC} of 27.8 mA/cm^2, compared to 25 mA/cm^2 from flat devices, demonstrating a plasmonic enhancement to the device performance achieved by incorporating nanostructures in the rear active layer/Au electrode interface.

UV photodetectors are important in a variety of applications including environmental monitoring, scientific research, imaging, and flame and missile detection.[7,15,16] However, plasmonic enhancement mechanisms have not been widely applied to optoelectronic devices in the UV spectral range. Unlike the common plasmonic metals of Ag and Au, which work well in the visible and near-infrared spectral ranges, Al is well-suited to support and tune SPPs in the UV spectral range due to its carrier concentration and dielectric function.[17−23] Organic UV photodetectors with a conventional device structure typically have Al as the top electrode, deposited by thermal evaporation. Therefore, incorporating nanostructures at the rear surface of the active layer inherently produces an Al nanostructure array that can utilize the unique UV plasmonic properties of Al and enhance UV photodetector performance.

In this work, nanohemisphere arrays (NHSAs) were imprinted into the top active layer surface in conventional organic UV photodetectors and were transferred to the top Al cathode to generate plasmonic Al nanostructures. The impact of plasmonic NHSA on device performance was investigated using both 3-dimensional finite-difference time-domain (3D-FDTD) electromagnetic simulations and experimental methods. The wide band gap polymer poly(9,9-dioctylfluorene-*alt*-bithiophene) (F8T2) was blended with $PC_{71}BM$ in a weight ratio of 100:4 and used as the active layer. Conventional UV photodetectors with this weight ratio demonstrated photomultiplication under large reverse biases.[8] The active layer thickness, which has a significant impact on device performance with regards to the spectral selectivity,[24−26] strength,[9] and photoresponse stability,[8] was varied between 125 and 470 nm. For comparison, devices with flat top active layers and electrodes were also investigated. 3D-FDTD simulations revealed that the devices with plasmonic NHSA top electrodes, referred to in this work as NHSA-top devices, exhibit stronger UV absorption in the active layer and enhanced electric fields at the interface of the top of the active layer and the Al electrode, especially for devices with thinner active layers. NHSA-top devices were fabricated by imprinting nanostructured molds into the top surface of the active layer, followed by thermal evaporation of the LiF electron transport layer and Al electrode, and evaluated alongside flat-top control devices whose active layers were imprinted with flat molds. The inclusion of a NHSA was found to improve the photoresponse strength, sensitivity and speed through increased UV absorption and enhanced electric fields resulting from angular reflection of light in the active layer and the plasmonic effects of the Al NHSA electrode. This work demonstrates that imprinting an NHSA into the top of the active layer, thus structuring the top metal electrode, is an effective approach for incorporating performance-enhancing plasmonic nanostructures into organic UV photodetectors.

DOI: 10.1021/acsanm.9b01586
ACS Appl. Nano Mater. 2019, 2, 6690−6700

EXPERIMENTAL SECTION

3-D FDTD Simulation. Three-dimensional, finite-difference time-domain (3D-FDTD) electromagnetic simulations (Lumerical, Inc.[27]) were used to investigate the incorporation of NHSA-tops on the light absorption in the active layer and the internal electric field distribution throughout the device. The simulated device structure was Corning XG EAGLE glass (100 nm)/ITO (200 nm)/PEDOT:PSS (40 nm)/F8T2:$PC_{71}BM$ (100:4, w:w, varied thickness)/LiF (0.8 nm)/Al (100 nm) (Figure 1a). The active layer is composed of a planar bulk portion with a hexagonal array of nanohemispheres, 200 nm in diameter (D), incorporated at its top surface. The thicknesses of the planar portion of the active layer were 100, 205, 355, and 445 nm (see Figure S1 for details about the determination of these thicknesses and the comparison to the flat-top active layer thicknesses). The hexagonal array of nanohemispheres was subsequently incorporated into the LiF and Al layers. A cross-sectional and top-view of the simulation unit cell are provided in Figures 1b and 1c, respectively. The simulation unit cell is defined by the blue border in Figures 1b and 1c and has the x- and y-lattice constants of D and $D\sqrt{3}$, respectively. The light source was placed 600 nm below the glass substrate and impinged normally with polarization in the x-direction. For comparison, flat-top devices were simulated with the same configuration and unit cell with active layer thicknesses of 125, 230, 380, and 470 nm. The wavelength-dependent refractive index (n) and extinction coefficient (k) of each material, and other simulation details were the same as those used in our previous work.[28]

Horizontal frequency-domain field monitors (light blue lines in Figure 1b) were placed throughout the device between planar layers, at the top of the device, and below the light source to calculate the absorbance in planar layers, device transmittance, and device reflectance, respectively. Absorbance in planar device layers was calculated by subtracting the transmittance above the layer from the transmittance below it. In NHSA-top devices, the relative absorbance within device active layers was determined from the device reflectance, transmittance, and absorbance in the layers below the active layer, by eq 1:

$$A_{\mathrm{ACTIVE}} = 1 - R - T - A_{\mathrm{ITO}} - A_{PEDOT:PSS} - A_{\mathrm{GLASS}} \quad (1)$$

where A_{ACTIVE} is the absorbance of the device active layer, R is the total reflectance from the device, T is the transmittance through the top of the device, and A_{ITO}, $A_{\mathrm{PEDOT:PSS}}$, and A_{GLASS} are the absorbance in the ITO electrode, PEDOT:PSS layer and glass substrate, respectively.

Vertical frequency-domain field monitors (dashed yellow lines in Figure 1b,c) were placed in the x−z and y−z planes of the device, intersecting at the origin (0,0), which corresponds to the center of the central nanohemisphere in the unit cell, to obtain the electric field distribution throughout the device under 330 nm monochromatic illumination. Electric field distributions were also mapped along the z-axis at individual x−y points and plotted against incident wavelength. For NHSA-top devices, three x-y points were used to accurately represent the electric field, since both the device geometry and internal electric field vary along x and y. These points, corresponding to the center of a nanohemisphere (0, 0), the x-edge of a nanohemisphere (D/2, 0), and the y-edge of a nanohemisphere (0, D/2) are marked in Figure 1c by pink, blue, and green stars, respectively. For flat-top devices, one x−y point was plotted (0, 0) since all x−y points are identical.

NHSA Mold Fabrication and Imprinting into the Top Surface of the Active Layer. To fabricate the mold for NHSA imprinting, nanosphere monolayers were first deposited on bare glass substrates, by the same procedure described in our previous work.[28] To aid in the eventual mold separation, the antiadhesive material trichloro(1H,1H,2H,2H-perfluorooctyl)silane (97%, Sigma-Aldrich, St. Louis, MO) was deposited on the hexagonal nanosphere monolayers by placing glass substrates covered with the monolayers and a separate dish containing 200 μL silane in a vacuum desiccator for 2 h. Polydimethylsiloxane (PDMS, Sylgard 184, Thermo Fisher Scientific, Waltham, MA) was poured over the treated nanosphere monolayers, degassed in a desiccator for 15 min, and cured at 70 °C for 5 h on a hot plate. After curing, the PDMS was separated from the nanosphere monolayer, producing a mold with a hexagonal array of 200 nm diameter hemispheric dimples. Flat molds were prepared by pouring PDMS on a silane-treated bare glass substrate. To imprint the NHSA onto the top surface of the active layer, the NHSA PDMS molds, wetted with 20 μL of 1,2-dichlorobenzene (anhydrous, 99.9% purity, Sigma-Aldrich, St. Louis, MO), were placed on F8T2:$PC_{71}BM$ films immediately after they were annealed at 80 °C for 10 min, remained on the hot plate at 80 °C for 5 min, and were then removed. The flat PDMS mold was imprinted onto the top of active layers by the same method to produce flat-top active layers for control devices.

Device Fabrication and Characterization. ITO-coated glass substrates (≤10 Ω/sq, Colorado Concept Coatings LLC, Loveland, CO) were cleaned and coated with a PEDOT:PSS (Clevios P VP AI 4083, Heraeus, Hanau, Germany) hole transport layer.[28] In a nitrogen-filled glovebox, F8T2 (molecular weight of 29000 g/mol, polydispersity index of 3.3, American Dye Source, Baie D'Urfe, Quebec, Canada) and $PC_{71}BM$ (Nano-C Inc., Westwood, MA) were each dissolved in 1,2-dichlorobenzene and stirred at 700 rpm and 70 °C for at least 12 h. The equal concentration F8T2 and $PC_{71}BM$ solutions were mixed in a F8T2:$PC_{71}BM$ weight ratio of 100:4 to yield precursor solutions with total concentrations of 20, 30, and 40 mg/mL, which were stirred at 700 rpm and 70 °C for at least 1 h and then filtered through a 0.2 μm PTFE syringe filter. Active layers with the target film thicknesses of 125, 230, 380, and 470 nm were produced by spinning 20, 30, 40, and 40 mg/mL precursor solutions at 1000, 1000, 1000, and 800 rpm, respectively for 30 s, and annealing at 80 °C for 10 min. A NHSA or flat PDMS mold was imprinted on the top surface of each active layer following the method described above. UV−vis absorption spectra were collected using a PerkinElmer Lambda 900 UV−vis spectrophotometer. Film thickness was measured using a Bruker OM-DektakXT profilometer. A thin 0.8−1.0 nm layer of LiF (99.995%, Sigma-Aldrich) was then deposited via thermal evaporation, without the use of any mask. Finally, 100 nm Al electrodes were deposited via thermal evaporation through a mask with 16 circular holes to generate 16 devices per substrate with each having an 0.03 cm^2 active area. Both LiF and Al were deposited using an Angstrom Engineering PVD Platform, with stage rotation turned on to avoid any shadowing effects on the NHSA-tops, and thickness was monitored by a quartz crystal microbalance. All device and film characterizations were performed in air. Current density−voltage (J−V) curves, dark current over time, external quantum efficiency (EQE) spectra, and response speed were measured using a Keithley 2635B sourcemeter. Light was provided using a Xenon arc lamp (150 W) and Oriel Cornerstone 130 monochromator. Optical intensity was measured using a Newport 1918-R Power Meter and Newport UV−Si photodiode. The response speed was obtained by manually switching between dark and light conditions. Matlab was used to perform fast Fourier transforms on dark current over time data to obtain noise currents.

RESULTS AND DISCUSSION

Investigating the NHSA-Top Impact in 3D-FDTD-Simulated Devices with Varied Active Layer Thickness. Three-dimensional finite-difference time-domain (3D-FDTD) electromagnetic simulations were performed to evaluate the impact of NHSA-tops on the absorbance and electric field distribution in the active layers of conventional UV photodetectors with the configuration shown in Figure 1a. NHSA-top devices have active layers composed of a planar portion with a NHSA incorporated into the top surface. The thicknesses of the planar portions were 100, 205, 305, and 455 nm and the diameter of the nanohemispheres was 200 nm. Accounting for the topography of nanohemispheres in the overall film thickness, corresponding flat-top active layer thicknesses of 125, 230, 380, and 470 nm, respectively, were

DOI: 10.1021/acsanm.9b01586
ACS Appl. Nano Mater. 2019, 2, 6690−6700

used. Details regarding the simulated and experimental active layer structure and thickness can be found in the Supporting Information (Figure S1). To simplify the discussion throughout, we use the flat-top active layer thickness to indicate the active layer thickness for both flat- and NHSA-top devices and refer to 125 and 470 nm active layers as thin and thick devices, respectively, while 230 and 380 nm active layers are termed intermediate devices.

The active layer absorbance (A_{ACTIVE}) and device reflectance (R) for devices with both NHSA- and flat-tops were calculated and are shown in Figure 2 for thin and thick devices and in

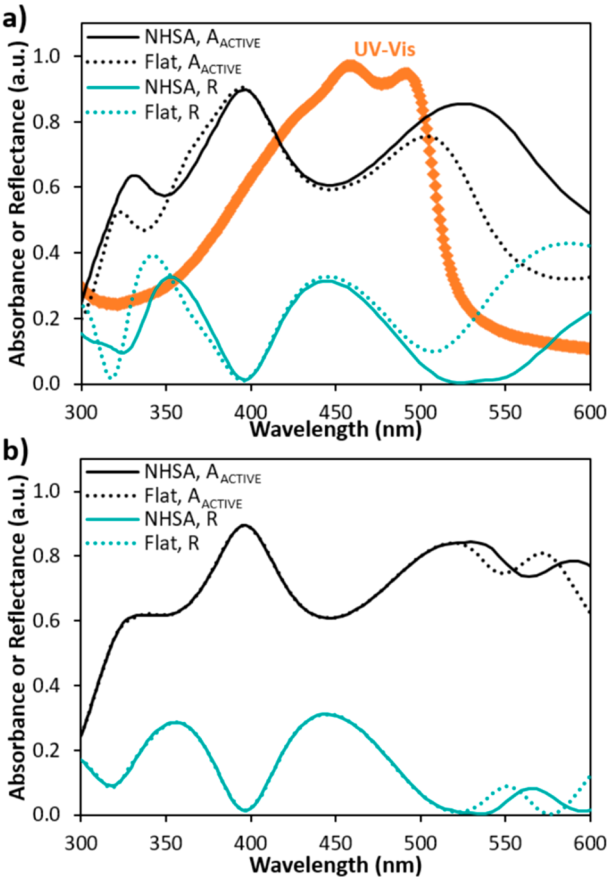

Figure 2. 3D-FDTD-simulated active layer absorbance (A_{ACTIVE}) and total device reflectance (R) for NHSA- and flat-top devices with (a) thin and (b) thick active layers. An experimentally obtained UV−vis absorption spectrum is superimposed in (a).

Figure S2a,b for intermediate devices. The simulated absorbance in the device layers below the active layer, PEDOT:PSS and ITO, is shown for all devices in Figure S2c,d. The peaks and dips exhibited throughout both the A_{ACTIVE} and R spectra are attributed to the reflectance between layers and nanocavity effects that exist in any device composed of multiple thin layers, as some portion of light is reflected at each interface between layers and these reflections create optical interference throughout the device. These could be minimized by adding antireflection coating on the glass substrate or at the rear of the active layer or by manipulating the substrate refractive index and device layer thicknesses.[29]

The results in Figure 2 show that the thin device is more significantly affected by NHSA-top incorporation than the thick device, and Figure S2a,b demonstrates that the influence of NHSA-top on active layer absorbance gradually diminishes with increasing active layer thickness. For the 125 nm active layer (Figure 2a), NHSA- and flat-top devices produce reflectance values of 0.11 and 0.25, respectively, under 330 nm illumination, demonstrating that the NHSA-top provides a significant reflectance reduction. Consequently, the NHSA-top device has a higher absorbance of 0.63 compared to the flat-top device, which has an absorbance of 0.50, under 330 nm illumination. The enhanced absorbance for NHSA-top devices was also observed under long-wavelength incident illumination because the behavior in the spectral region beyond ∼530 nm is dominated by reflectance of the top electrode. As demonstrated by the experimentally measured UV−vis absorption spectrum of F8T2:$PC_{71}BM$ (100:4, w:w) included in Figure 2a, the active layer does not have significant absorption in this spectral region. To confirm that the structuring of the active layer/LiF/Al interface causes the enhanced UV absorption observed in Figure 2a, rather than the structuring of the polymer film itself, UV−vis absorption spectra were obtained for thin NHSA- and flat-top films without the subsequent layers deposited, and these are shown in Figure S3. Clearly, NHSA incorporation does not impact the absorption of the active layer film by itself, so the impact observed in Figure 2a results from the structuring of the active layer/LiF/Al interface. For the thick device (Figure 2b), the impact of NHSA-tops on active layer absorbance virtually disappears, and the simulated absorbance and reflectance of NHSA- and flat-top devices are identical except for minor differences under long-wavelength illumination.

To better explain and understand the impact that NHSA incorporation may have on device performance, the internal electric field distributions in simulated NHSA- and flat-top devices were evaluated and are presented in Figures 3 and 4. In Figure 3, the electric field distribution under 330 nm illumination, which corresponds to a peak in active layer absorbance, is mapped in the $x-z$ and $y-z$ cross sections of NHSA-top devices and the $x-z$ cross-section of flat-top devices. Figures 3a and 3b show the electric field distributions in the active layers and subsequent top layers for thin and thick devices, respectively. The LiF electron transport layer was included in the simulations but is too thin (0.8−1.0 nm) to be seen clearly in Figure 3. The electric field distributions under the same conditions for the intermediate devices are shown in Figure S4a,b. Again, the impact of the NHSA-top on the electric field distribution is most significant for the thin device and gradually decreases as active layer thickness increases.

Figure 3a shows that strong electric fields are confined in the nanohemispheric region of the active layer in the thin device and extend to the edge of the active layer/LiF/Al electrode interface in the $x-z$ cross section because incident light is polarized in the x-direction. Although the flat-top thin device shows a similar electric field intensity, the high-intensity region is more concentrated toward the middle of the active layer, away from the Al interface. As shown in Figure S4a,b, the intensity of the confined electric field in the nanohemispheric active layer region deceases gradually with increasing active layer thickness. For the thick device, this confinement is almost completely diminished, and the electric field distribution for the thick NHSA-top device is very similar to that of the flat-top device. Clearly, NHSA-tops provide a plasmonic enhancement to the electric field intensity at the active layer/LiF/Al interface, especially for thinner devices. The enhanced electric field could improve charge separation, transport, and injection

DOI: 10.1021/acsanm.9b01586
ACS Appl. Nano Mater. 2019, 2, 6690−6700

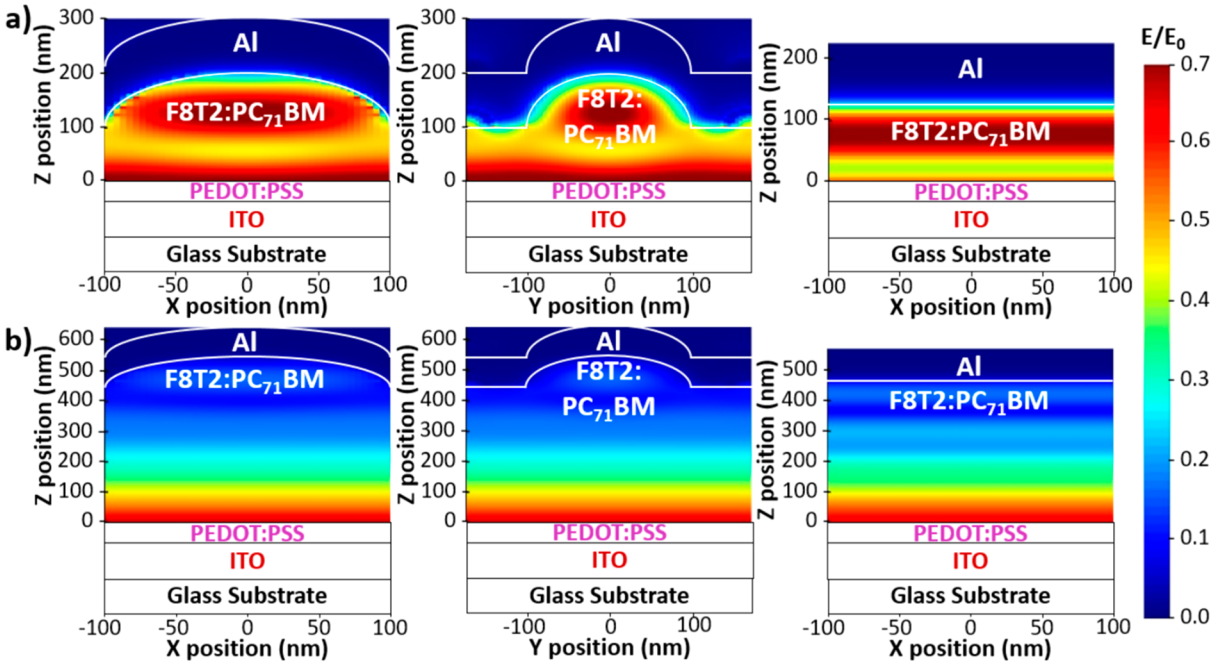

Figure 3. 3D-FDTD simulated electric field distributions, under 330 nm illumination, of the x-z cross section ($y = 0$) and y-z cross section ($x = 0$) in NHSA-top devices and the x-z cross-section ($y = 0$) in flat-top devices with (a) thin and (b) thick active layers. The color scale is consistent for all plots and represents the ratio of the electric field intensity (E) to the incident field (E_0), which has an intensity of 1 V/m.

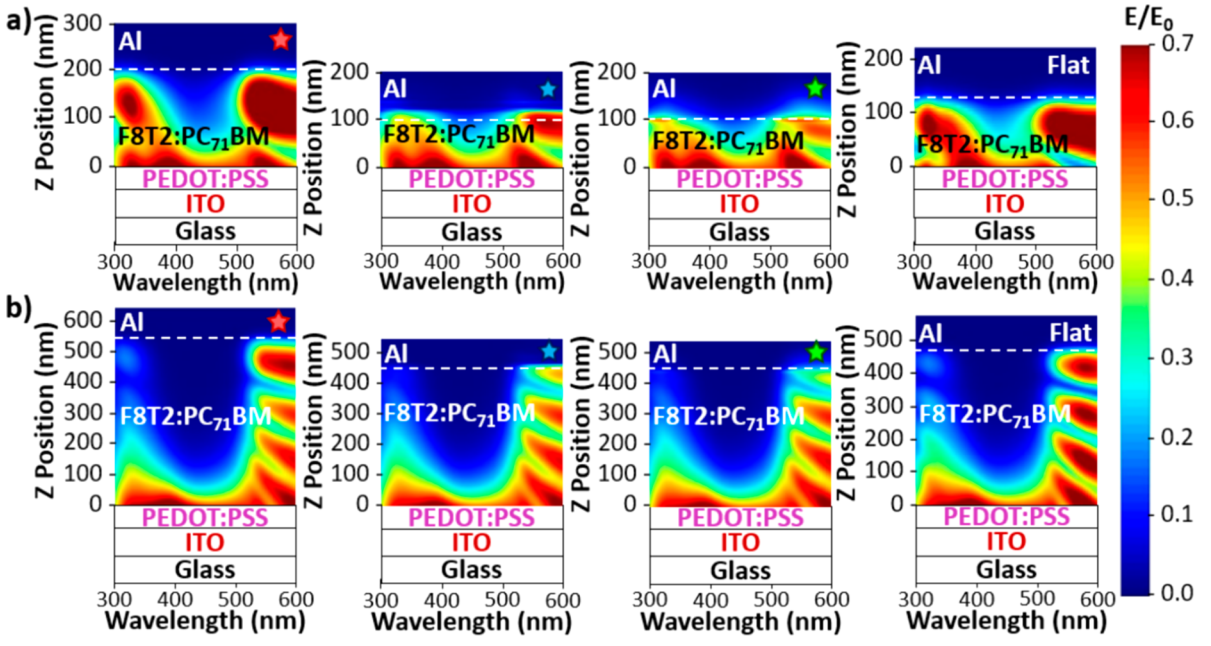

Figure 4. 3D-FDTD-simulated electric field distributions at a single x–y point, mapped along the z-axis against incident wavelength for both NHSA- and flat-top devices with (a) thin and (b) thick active layers. From left to right across each panel, electric field distributions are shown at the center ((0, 0), marked by a pink star), x-edge ($(D/2, 0)$, marked by a blue star), and y-edge ($(0, D/2)$, marked by a green star) of the central nanohemisphere in NHSA-top devices and at any x–y point in a flat-top device. The color scale is consistent for all plots and represents the ratio of the electric field intensity (E) to the incident field (E_0), which has an intensity of 1 V/m.

at the top of device active layers and subsequently improve the photoresponse strength and speed.[5,7]

Internal electric field distributions were also mapped along the z-axis, at individual x–y points, and plotted against incident wavelength in the spectral range of 300–600 nm so that the relationship between electric field intensity and the wavelength of incident light could be investigated. The resulting plots are shown in Figures 4a and 4b for thin and thick devices, respectively. Because both the geometry and electric field distribution vary across the NHSA-top devices, while they are uniform in flat-top devices, three distinct points are included for NHSA-top devices while a single point is used for flat-top devices. The three points plotted for NHSA-top devices correspond to the center, x-edge, and y-edge of the central nanohemisphere and are marked by pink, blue, and green stars, respectively, in Figures 1c and 4. These center, x-edge, and y-

DOI: 10.1021/acsanm.9b01586
ACS Appl. Nano Mater. 2019, 2, 6690–6700

edge points correspond to the coordinates of (0, 0), (D/2, 0), and (0, D/2) based on the coordinate system defined in Figure 1c. The same plots, marked in the same way, are shown in Figure S4c,d for intermediate devices.

As observed in Figure 4, the thin device exhibits a stronger electric field than the thick device, especially in the top portion of the active layer in the spectral ranges of 300−350 and 530−600 nm. The fringes in the electric field intensity observed in the spectral range between 530 and 600 nm occur because this light is beyond the absorption range of the active layer (Figure S3), so it penetrates the active layer and reflects off the top electrode, establishing an interference pattern throughout the active layer. Because this light will not contribute to the photoresponse of fabricated devices, our discussion focuses on the UV spectral range, which is more relevant for understanding and predicting experimental results. In the center of the nanohemisphere of the thin device, marked by a pink star in Figure 4a, the highest intensity area is located near the middle of the nanohemispheric region of the active layer, between z values of about 100 and 200 nm, and the intensity decreases toward the active layer/LiF/Al electrode interface under incident illumination between about 300 and 350 nm. The thin flat-top device exhibits a similar electric field distribution. However, at the x- and y-edges of the nanohemisphere, marked by blue and green stars, respectively, the strongest electric field occurs directly at the active layer/LiF/Al electrode interface under incident illumination with wavelengths between about 330 and 350 nm, indicating UV-selective plasmonic enhancements to the local electric field. The strong local electric fields at the x- and y-edges of the nanohemisphere at the active layer/LiF/Al electrode interface can be seen in Table 1, which summarizes the ratios of E/E_0, under 330 nm illumination, for each device at three x−y points for NHSA-top devices and a single x−y point for flat-top devices.

Table 1. Summary of the Ratios of E/E_0 at the Active Layer/LiF/Al Electrode Interface for All Simulated Devices under 330 nm Illumination at Three x−y Points for NHSA-Top Devices and a Single x−y Point for Flat-Top Devices

	E/E_0 under 330 nm illumination			
average active layer thickness (nm)	center of hemisphere	x-edge of hemisphere	y-edge of hemisphere	flat-top
125	0.17	0.44	0.53	0.27
230	0.12	0.28	0.33	0.17
380	0.063	0.14	0.17	0.091
470	0.042	0.095	0.11	0.060

With increasing active layer thickness, the electric field intensity decreases under illumination with wavelengths between about 300 and 350 nm as shown in Figure S4c,d and Table 1 for the intermediate devices with the active layer thickness of 230 and 380 nm, respectively. For the thick devices shown in Figure 4b, the electric field intensities at the active layer/LiF/Al electrode interface for the NHSA-top device at three x−y points and for the flat-top device at one x−y point are relatively weak under illumination with wavelengths between about 300 and 350 nm. Similar to thin and intermediate devices, the electric field at the center of the nanohemisphere exhibits similar behavior to flat-top devices, but the electric field at the edges of the nanohemisphere is enhanced due to localized surface plasmon resonance induced by the NHSA Al top electrodes, which can be seen in Table 1.

Fabrication of NHSA- and Flat-Top Devices by Nanoimprinting. 3D-FDTD simulation results clearly show the plasmonic effect of the NHSA top Al electrode in the increase of UV absorption in the active layer and the enhancement of the electric field at the active layer/LiF/Al electrode interface under UV illumination, especially for the thin device. We therefore fabricated photodetectors with both NHSA- and flat-top active layers, inherently incorporating the NHSA into the subsequent LiF and Al layers, and evaluated their performance. The procedure for fabricating and imprinting NSHA molds into device active layers to produce NHSA-top devices is summarized in Figure 5. It has been reported that the imprinting procedure alone, regardless of whether a flat or patterned mold is used, can have an impact on the active layer morphology and thus affect the device performance,[30] so control flat-top devices in this work were imprinted with a flat mold by the same procedure that is illustrated in Figure 5.

Many previous works have realized pattern transfer to the top surface of the active layer by applying temperature and pressure during imprinting.[30−32] Because the active layer in this work was composed of a 100:4 weight ratio blend of the soft polymer F8T2 and organic molecule $PC_{71}BM$, the film could be imprinted by wetting the PDMS mold with the same solvent used for dissolving the active layer components and placing the mold on the film without applying pressure or any additional temperature beyond the annealing temperature. The NHSA, consisting of hexagonally arranged 200 nm diameter nanohemispheres, was successfully incorporated into the top surface of the active layer and transferred to the thermally deposited LiF electron transport layer and top Al electrode, as shown in the SEM images included in Figure 5.

Because active layer film thickness is known to impact device performance,[8,9,24−26] the NHSA- and flat-top active layers with target thicknesses of 125, 230, 380, and 470 nm were fabricated, and the thicknesses of NHSA- and flat-top films were compared. As shown in Figure S1b, the average thicknesses of NHSA-top films are very close to the flat-top target film thicknesses, so film thickness will not be considered as contributing to any difference in performance between NHSA- and flat-top devices.

Evaluating the Performance of NHSA- and Flat-Top Devices with Thin and Thick Active Layers. NHSA- and flat-top devices, with an overall device structure of ITO/PEDOT:PSS/F8T2:$PC_{71}BM$ (100:4)/LiF/Al were fabricated with the four target active layer thicknesses. Because the 3D-FDTD simulations show that the active layer absorbance and electric field behavior gradually change with increasing active layer thickness, we focused the evaluation on the thin (125 nm) and thick (470 nm) devices with both NHSA- and flat-tops. Current density−voltage characteristics for thin and thick devices are provided in Figures 6a and 6b, respectively, both in the dark and under monochromatic 330 nm illumination. For thin devices (Figure 6a), the magnitudes of the photocurrent density produced by NHSA- and flat-top devices are similar, but NHSA-top devices produce lower dark current density. As observed in Figure 6b, the dark current density of thick devices is about 1−2 orders of magnitude lower than that of thin devices because the series resistance and charge extraction difficulty increase with increasing active layer thickness.[7] Dark and photocurrent densities of thick NHSA-top devices are

DOI: 10.1021/acsanm.9b01586
ACS Appl. Nano Mater. 2019, 2, 6690−6700

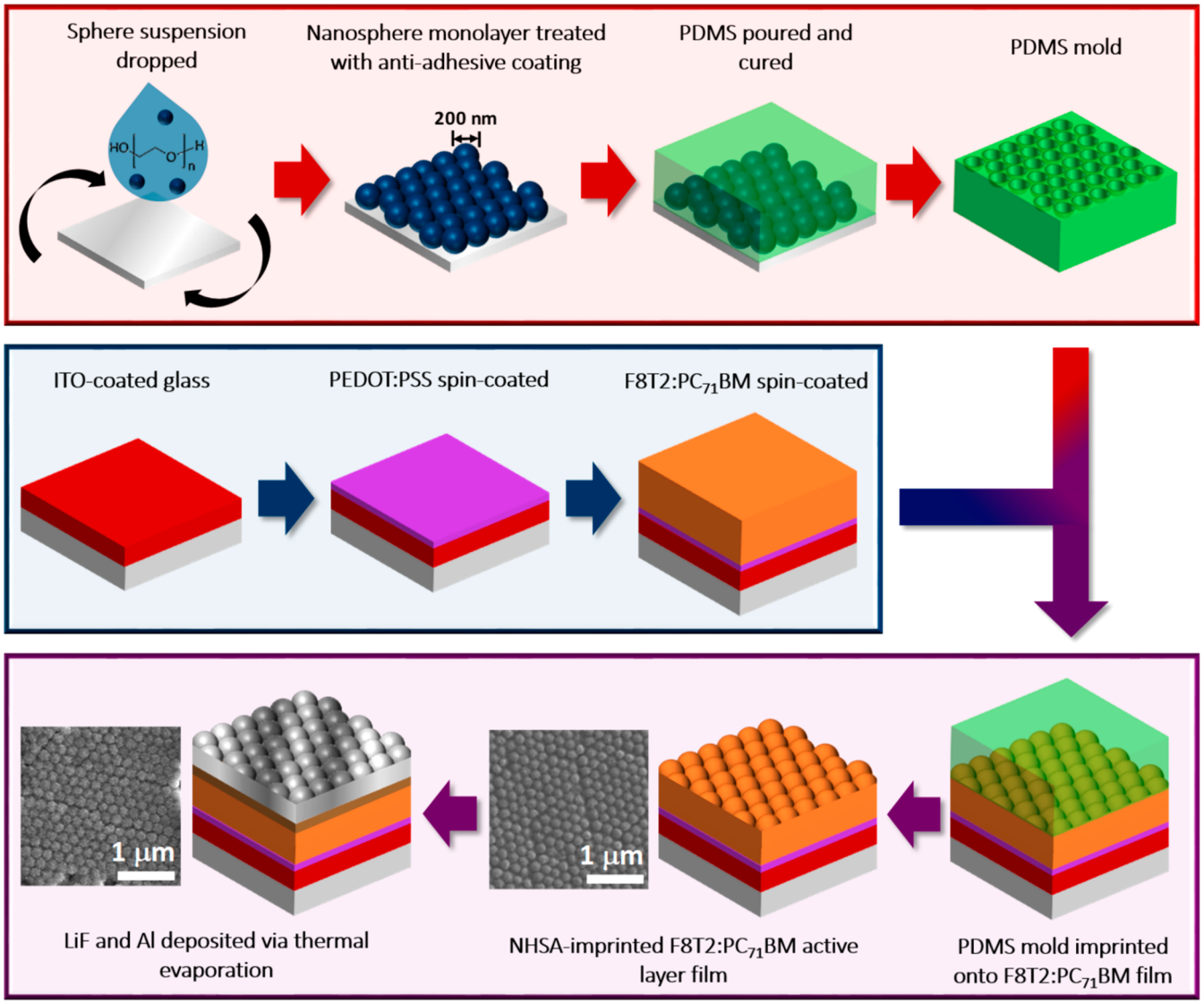

Figure 5. Schematic of the procedure for making NHSA PDMS molds, imprinting into the top surface of active layers, and transferring to LiF and Al top electrodes. The SEM images of the NHSA-top active layer and the NHSA-top Al electrode are included in the bottom panel.

slightly higher than those of flat-top devices. For both thin and thick devices, incorporating the NHSA-top results in shifts in the voltages where the minimum dark and illuminated current are obtained, termed V_0 and open-circuit voltage (V_{OC}), respectively. For thin devices (Figure 6a), NHSA- and flat-top devices exhibit V_{OC} values of 0.76 and 0.24, respectively, while the V_0 values are both close to 0 V, and for thick devices (Figure 6b) NHSA- and flat-top devices exhibit V_0 values of −0.48 and −0.08, respectively, and similar V_{OC} values of 0.20 and 0.32 V, respectively. These shifts may be indicative of an additional built-in bias related to the electric field enhancements provided by plasmonic NHSA-tops. It is also hypothesized that these shifts could be related to changes in the microstructure and morphology at the top interface of the active layer because the V_{OC} in organic photodiodes is known to depend on the active layer materials and morphology, interfacial layers, and the nature of the electrode contacts.[33−36]

External quantum efficiency (EQE) spectra of thin and thick devices are shown in Figures 6c and 6d, respectively, and represent the ratio of charge carriers produced by a device to photons incident on the device, thereby indicating the photoresponse strength. The spectra in Figures 6c and 6d exhibit a consistent spectral shape with peaks around 330 and 515 nm, corresponding to the edges of the active layer absorption peak (Figure S3). Light at these wavelengths is absorbed weakly, enabling it to penetrate the active layer and be absorbed at the top of the device. Because $PC_{71}BM$ clusters are known to be more concentrated at the top of the active layer, light absorbed in this physical region can most effectively engage the reverse-bias photoresponse mechanism.[8] For thick devices, a pronounced dip corresponding to the active layer absorbance peak, between about 400 and 500 nm, is observed in the EQE spectra in Figure 6d. Light within this spectral region is absorbed quickly and therefore has a low penetration depth, precluding it from reaching the top of the active layer and contributing significantly to photoresponse as previously observed.[8,9] This agrees with the 3D-FDTD-simulated electric field distributions shown in Figure 4b, which demonstrate that the electric field in the spectral range between about 400 and 500 nm is strong at the bottom of the active layer and decays quickly with depth into the active layer.

DOI: 10.1021/acsanm.9b01586
ACS Appl. Nano Mater. 2019, 2, 6690−6700

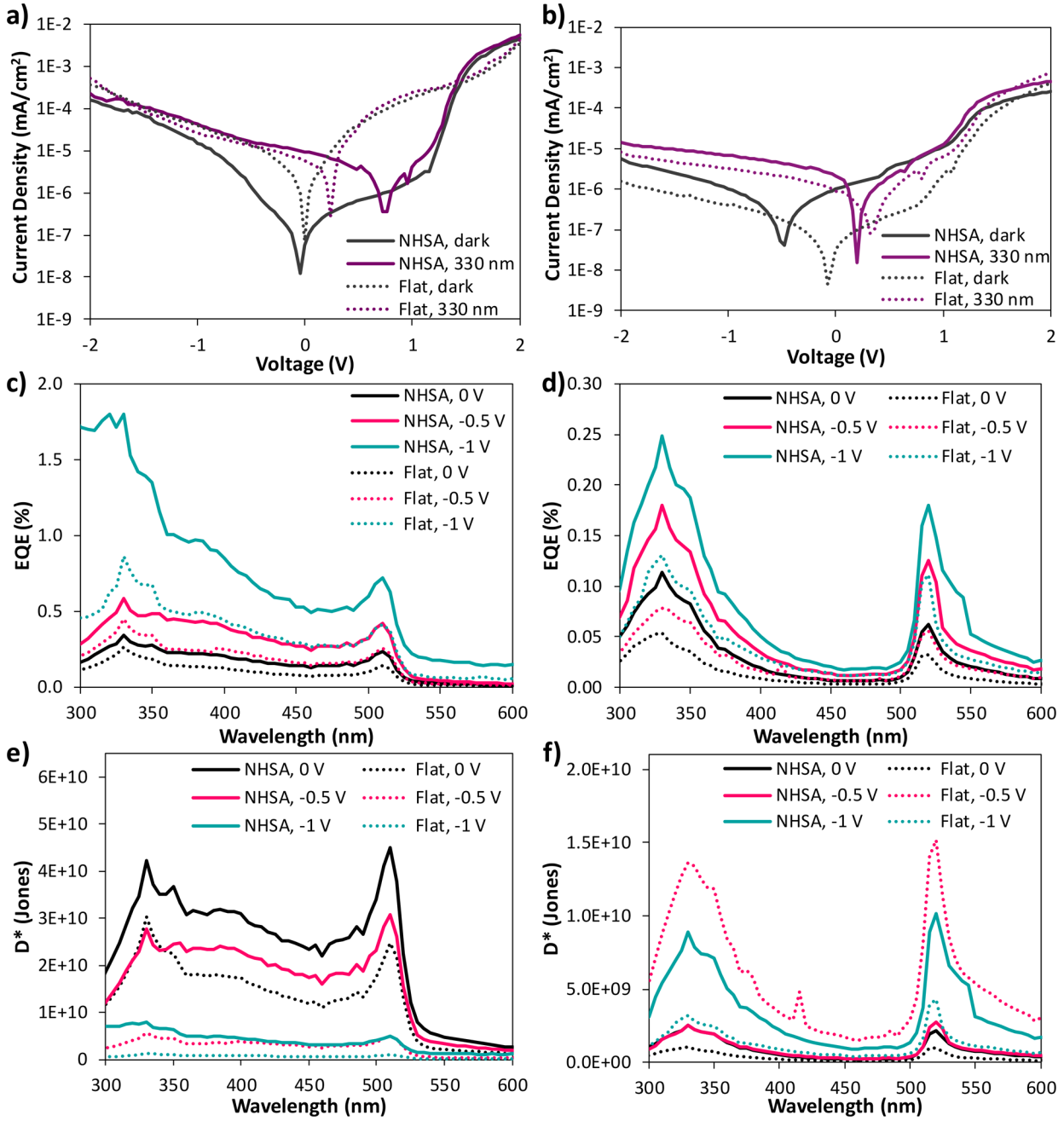

Figure 6. (a, b) Current density−voltage characteristics, (c, d) EQE spectra, and (e, f) *D** spectra for (a, c, e) thin and (b, d, f) thick devices.

For both NHSA- and flat-top devices, EQE increases with increasing reverse bias. Regardless of the active layer thickness and the bias applied, NHSA-top devices produce higher EQE values than flat-top devices, indicating that the nanostructures achieve the desired performance enhancement. Under a −1 V bias and 330 nm illumination, thin NHSA- and flat-top devices produce peak EQE values of 1.8 and 0.86%, and thick NHSA- and flat-top devices produce EQE values of 0.25 and 0.13%, respectively. The photoresponse strength is diminished for thicker devices due to the increased difficulty of charge extraction from thicker active layers.[7] It should be noted that the significant increase in EQE values produced by the thin NHSA-top device under a −1 V bias and illumination with increasingly short wavelengths is an indication that the device is approaching unstable behavior, because the lamp power in this spectral region (Figure S5) is very weak. The spectrum levels off at a reasonable value, so this data is still reliable, but this is considered the reverse-bias limit of device stability for the thin device. Devices with the same structure but thicker active layers were previously shown to be stable under reverse biases as strong as −40 V,[8] so it is anticipated that the thick devices in this work would maintain stable behavior under strong reverse biases. However, increasing the reverse bias was found to diminish the NHSA-top impact because the strong applied bias overwhelmed the plasmonic enhancements to the internal electric field. Therefore, in the interest of maintaining stable behavior for all evaluated devices and examining the impact of NHSA-tops, our discussion focuses on device behavior under small applied reverse biases.

DOI: 10.1021/acsanm.9b01586
ACS Appl. Nano Mater. 2019, 2, 6690−6700

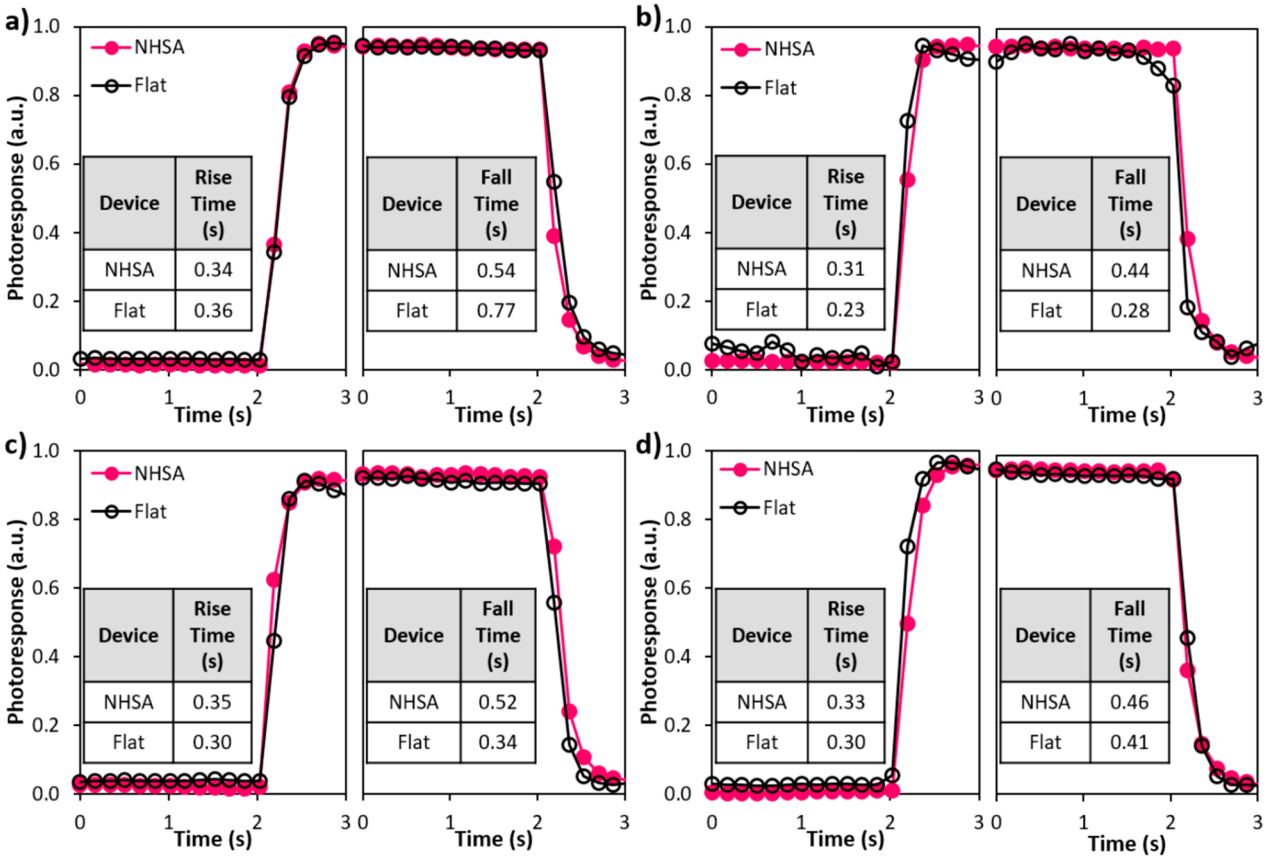

Figure 7. On−off response speed for (a, b) thin and (c, d) thick devices with both NHSA- and flat-tops. The response speed was measured under 330 nm illumination and (a, c) 0 V bias and (b, d) −0.5 V bias. The calculated rise and fall times are included as an inset in each plot.

The specific detectivity (D^*), which accounts for the noise within devices and therefore provides an indication of photoresponse sensitivity, was calculated by eq S1 and is provided for thin and thick devices in Figures 6e and 6f, respectively. Noise currents for thin and thick devices with NHSA- and flat-tops were obtained by performing a fast Fourier transform on measured dark current over time and are reported in Table S1. As shown in Figure 6e, thin NHSA-top devices exhibit consistently higher D^* values than flat-top devices, achieving peak D^* values of 4.2×10^{10} and 3.0×10^{10} jones, respectively, under 0 V bias and 330 nm illumination, which are competitive with those reported for other organic UV photodetectors.[37−39] In this case, the maximum D^* value is obtained without any applied bias because the noise current is minimized in this condition. For thick devices, NHSA-top devices exhibit higher D^* values than flat-top devices under 0 and −1 V biased, with peak D^* values of 8.9×10^9 and 3.2×10^9 jones, respectively, under −1 V bias and 330 nm illumination. However, NHSA-top devices exhibit lower D^* values than flat-top devices under −0.5 V bias due to a higher noise current (Table S1). Thick flat-top devices achieve the maximum D^* value of 1.4×10^{10} jones under −0.5 V bias and 330 nm illumination.

The on−off response speeds of thin and thick devices with NHSA- and flat-tops were collected under 0 and −0.5 V bias and 330 nm illumination and are shown in Figure 7 along with calculated rise and fall times for each device and testing condition. In general, the response times exhibited by these devices are relatively slow compared to the broader field of photodetection, primarily because of the multistep photoresponse mechanism, relying on an initial, slow step of charge trapping that these devices employ.[8,9] The response speed could be improved by increasing the bias applied during operation, but in these devices the plasmonic effects of the NHSA-tops were overwhelmed when strong biases were applied, and as the primary objective of this work was to investigate the impact of NHSA incorporation, stronger biases were therefore avoided. As shown in Figure 7a, without any applied bias, thin NHSA-top devices respond faster than flat-top devices, with rise (fall) times of 0.34 s (0.54 s) and 0.36 s (0.77 s), respectively. The rise times are similar in magnitude, while the fall time is significantly shorter for the NHSA-top device than the flat-top device. The faster photoresponse might be attributed to the plasmonic enhancements to the electric field (Figures 3a and 4a), which acts as a small built-in bias. Increasing the bias applied to a device improves its response speed due to faster charge carrier transport and decreased capacitance.[7] In fact, when a −0.5 V bias is applied (Figure 7b), the overall response speed increases, and NHSA- and flat-top devices exhibit rise (fall) times of 0.31 s (0.44 s) and 0.23 s (0.28 s), respectively.

For thick devices, the plasmonic enhancement to the response speed is not clearly observed. Without any applied bias, shown in Figure 7c, NHSA- and flat-top devices exhibit similar rises times of 0.35 and 0.30 s, respectively, while the NHSA-top device fall time of 0.52 s is slower than the 0.34 s fall time of the flat-top device. When the bias is increased to −0.5 V (Figure 7d), the response speed is very similar for both NHSA- and flat-top devices, which exhibit rise (fall) times of 0.33 s (0.46 s) and 0.30 s (0.41 s), respectively. It is

DOI: 10.1021/acsanm.9b01586
ACS Appl. Nano Mater. 2019, 2, 6690−6700

hypothesized that the similarity of the response speeds for thick NHSA- and flat-top devices is related to the internal electric field distributions, which were relatively similar for thick NHSA- and flat-top devices (Figures 3b and 4b), so the response speed of NHSA-top devices does not benefit from this plasmonic effect.

The performance enhancement that the NHSA-tops provide can be attributed to two main factors. The first is angular light reflection that occurs when light that penetrates the active layer reflects off the NHSA nanostructured active layer/LiF/Al electrode interface at the top of the devices. Instead of reflecting straight back, as it does in flat-top devices, light is reflected at an angle, increasing its path length within the active layer and thereby improving light absorption within the active layer, as is demonstrated for the 3D-FDTD-simulated thin NHSA-top devices compared to the flat-top devices in Figure 2a. The second performance-enhancing effect of the NHSA-tops is provided through SPPs that occur at the nanostructured active layer/LiF/Al electrode interface. These localized surface plasmon resonances confine and enhance the local electric field in the nanohemispheric region of the active layer, as demonstrated in Figures 3 and 4. The enhanced electric field acts as a small, additional built-in bias, which improves both the photoresponse strength and sensitivity (Figure 6) and the on−off response speed (Figure 7).

CONCLUSIONS

Nanohemisphere arrays were incorporated into organic UV photodetectors by imprinting into the top surface of the active layer, and the pattern was then transferred to the LiF electron transport layer and top Al electrode. 3D-FDTD simulation results showed that NHSA-top devices with thin active layers exhibit a clear UV absorbance enhancement and strong confined electric fields in the nanohemispheric region of the active layer upon NHSA incorporation, in comparison to flat-top control devices. The impact of NHSA-tops on the absorbance and electric field in device active layers diminishes with increasing active layer thickness. NHSA molds were fabricated by nanosphere lithography and imprinted into device active layers, and devices with varied active layer thicknesses were fabricated and evaluated. Thin NHSA-top devices demonstrated superior performance compared to flat-top devices, producing peak D^* values of 4.2×10^{10} and 3.0×10^{10} jones, respectively, under 0 V bias and 330 nm illumination and faster on−off response speed. This work demonstrated that imprinting an NHSA into the top surface of the active layer is an effective method for incorporating plasmonic nanostructures into the top electrodes of organic ultraviolet photodetectors for improved photoresponse. This method can also be applied to incorporate plasmonic nanostructures into other optoelectronic devices to enhance device performance.

ASSOCIATED CONTENT

Supporting Information

The Supporting Information is available free of charge on the ACS Publications website at DOI: 10.1021/acsanm.9b01586.

Supplementary text, Figures S1−S5 and Table S1, containing detailed explanation of film thickness determination, 3D-FDTD-simulated and experimental results for devices with intermediate thicknesses, simulated absorbance in various device layers, experimental film absorption data, the optical power spectrum of the light source, and noise currents used to calculate specific detectivity (PDF)

AUTHOR INFORMATION

Corresponding Author

*E-mail qyu@uw.edu.

ORCID

Monica R. Esopi: 0000-0003-2262-4802

Qiuming Yu: 0000-0002-2401-4664

Notes

The authors declare no competing financial interest.

ACKNOWLEDGMENTS

The authors gratefully acknowledge financial support provided by the Defense Threat Reduction Agency (HDTRA1-15-1-0021) and the National Science Foundation (CMMI 1661660). Part of this work was conducted at the Molecular Analysis Facility, a National Nanotechnology Coordinated Infrastructure (NNCI) site at the University of Washington, which is supported in part by funds from the National Science Foundation (awards NNCI-1542101, 1337840, and 0335765), the National Institutes of Health, the Molecular Engineering & Sciences Institute, the Clean Energy Institute, the Washington Research Foundation, the M. J. Murdock Charitable Trust, Altatech, ClassOne Technology, GCE Market, Google, and SPTS. M.R.E. acknowledges a fellowship from the University of Washington Clean Energy Institute. Some device fabrication steps were performed in the University of Washington Department of Chemistry's Photonics Research Center. UV−vis absorption was conducted in the lab of Professor Samson Jenekhe.

REFERENCES

(1) Barnes, W. L.; Dereux, A.; Ebbesen, T. W. Surface plasmon subwavelength optics. *Nature* **2003**, *424* (6950), 824−830.

(2) Liang, Z. Q.; Sun, J.; Jiang, Y. Y.; Jiang, L.; Chen, X. D. Plasmonic Enhanced Optoelectronic Devices. *Plasmonics* **2014**, *9* (4), 859−866.

(3) Atwater, H. A.; Polman, A. Plasmonics for improved photovoltaic devices. *Nat. Mater.* **2010**, *9* (3), 205−213.

(4) Richardson, B. J.; Zhu, L.; Yu, Q. M. Design and development of plasmonic nanostructured electrodes for ITO-free organic photovoltaic cells on rigid and highly flexible substrates. *Nanotechnology* **2017**, *28*, 165401.

(5) Berini, P. Surface plasmon photodetectors and their applications. *Laser & Photonics Reviews* **2014**, *8* (2), 197−220.

(6) Liu, Y.; Lang, F.; Dittrich, T.; Steigert, A.; Fischer, C. H.; Kohler, T.; Plate, P.; Rappich, J.; Lux-Steiner, M. C.; Schmid, M. Enhancement of photocurrent in an ultra-thin perovskite solar cell by Ag nanoparticles deposited at low temperature. *RSC Adv.* **2017**, *7* (3), 1206−1214.

(7) Kasap, S. O. *Principles of Electronic Materials and Devices*; McGraw-Hill: New York, 2006.

(8) Esopi, M. R.; Calcagno, M.; Yu, Q. M. Organic Ultraviolet Photodetectors Exhibiting Photomultiplication, Low Dark Current, and High Stability. *Adv. Mater. Technol.* **2017**, *2* (8), 1700025.

(9) Li, L. L.; Zhang, F. J.; Wang, J.; An, Q. S.; Sun, Q. Q.; Wang, W. B.; Zhang, J.; Teng, F. Achieving EQE of 16,700% in P3HT: PC71BM based photodetectors by trap-assisted photomultiplication. *Sci. Rep.* **2015**, *5*, 9181.

(10) Li, L. L.; Zhang, F. J.; Wang, W. B.; Fang, Y. J.; Huang, J. S. Revealing the working mechanism of polymer photodetectors with

DOI: 10.1021/acsanm.9b01586
ACS Appl. Nano Mater. 2019, 2, 6690−6700

ultra-high external quantum efficiency. *Phys. Chem. Chem. Phys.* **2015**, *17* (45), 30712−30720.
(11) Miao, J. L.; Zhang, F. J. Recent progress on highly sensitive perovskite photodetectors. *J. Mater. Chem. C* **2019**, *7* (7), 1741−1791.
(12) Lee, Y. H.; Lee, T. K.; Kim, H.; Song, I.; Lee, J.; Kang, S.; Ko, H.; Kwak, S. K.; Oh, J. H. A Flexible High-Performance Photoimaging Device Based on Bioinspired Hierarchical Multiple-Patterned Plasmonic Nanostructures. *Small* **2018**, *14* (13), 1703890.
(13) Lan, W. X.; Wang, Y. W.; Singh, J.; Zhu, F. R. Omnidirectional and Broadband Light Absorption Enhancement in 2-D Photonic-Structured Organic Solar Cells. *ACS Photonics* **2018**, *5* (3), 1144−1150.
(14) Kim, Y.; Bicanic, K.; Tan, H. R.; Ouellette, O.; Sutherland, B. R.; de Arguer, F. P. G.; Jo, J. W.; Liu, M. X.; Sun, B.; Liu, M.; Hoogland, S.; Sargent, E. H. Nanoimprint-Transfer-Patterned Solids Enhance Light Absorption in Colloidal Quantum Dot Solar Cells. *Nano Lett.* **2017**, *17* (4), 2349−2353.
(15) Bhattacharya, P. *Semiconductor Optoelectronic Devices*; Prentice Hall: 1996.
(16) Baeg, K. J.; Binda, M.; Natali, D.; Caironi, M.; Noh, Y. Y. Organic Light Detectors: Photodiodes and Phototransistors. *Adv. Mater.* **2013**, *25* (31), 4267−4295.
(17) Knight, M. W.; King, N. S.; Liu, L. F.; Everitt, H. O.; Nordlander, P.; Halas, N. J. Aluminum for Plasmonics. *ACS Nano* **2014**, *8* (1), 834−840.
(18) Gong, T.; Munday, J. N. Aluminum-based hot carrier plasmonics. *Appl. Phys. Lett.* **2017**, *110* (2), 021117.
(19) Boltasseva, A.; Atwater, H. A. Low-Loss Plasmonic Metamaterials. *Science* **2011**, *331* (6015), 290−291.
(20) Cheng, C. W.; Liao, Y. J.; Liu, C. Y.; Wu, B. H.; Raja, S. S.; Wang, C. Y.; Li, X. Q.; Shih, C. K.; Chen, L. J.; Gwo, S. Epitaxial Aluminum-on-Sapphire Films as a Plasmonic Material Platform for Ultraviolet and Full Visible Spectral Regions. *ACS Photonics* **2018**, *5* (7), 2624−2630.
(21) Zhu, A. Y.; Kuznetsov, A. I.; Luk'yanchuk, B.; Engheta, N.; Genevet, P. Traditional and emerging materials for optical metasurfaces. *Nanophotonics* **2017**, *6* (2), 452−471.
(22) Ding, G.; Deng, J.; Zhou, L.; Gan, Q.; Hwang, J. C. M.; Dierolf, V.; Bartoli, F. J.; Mazuir, C.; Schoenfeld, W. V. Al nanogrid electrode for ultraviolet detectors. *Opt. Lett.* **2011**, *36* (18), 3663−3665.
(23) Taguchi, A.; Saito, Y.; Watanabe, K.; Yijian, S.; Kawata, S. Tailoring plasmon resonances in the deep-ultraviolet by size-tunable fabrication of aluminum nanostructures. *Appl. Phys. Lett.* **2012**, *101* (8), 081110.
(24) Esopi, M. R.; Zheng, E. J.; Zhang, X. Y.; Cai, C.; Yu, Q. M. Tuning the spectral response of ultraviolet organic-inorganic hybrid photodetectors via charge trapping and charge collection narrowing. *Phys. Chem. Chem. Phys.* **2018**, *20* (16), 11273−11284.
(25) Miao, J. L.; Zhang, F. J.; Du, M. D.; Wang, W. B.; Fang, Y. Photomultiplication type narrowband organic photodetectors working at forward and reverse bias. *Phys. Chem. Chem. Phys.* **2017**, *19* (22), 14424−14430.
(26) Armin, A.; Jansen-Van Vuuren, R. D.; Kopidakis, N.; Burn, P. L.; Meredith, P. Narrowband light detection via internal quantum efficiency manipulation of organic photodiodes. *Nat. Commun.* **2015**, *6*, 8.
(27) Lumerical, Inc. Material Database (Optical); https://kb.lumerical.com/en/materials_material_database_optical.html.
(28) Esopi, M. R.; Yu, Q. M. Plasmonic Aluminum Nanohole Arrays as Transparent Conducting Electrodes for Organic Ultraviolet Photodetectors with Bias-Dependent Photoresponse. *ACS Applied Nano Materials* **2019**, *2* (8), 4942−4953.
(29) Wang, B. M.; Ruud, C. J.; Price, J. S.; Kim, H.; Giebink, N. C. Graded-Index Fluoropolymer Antireflection Coatings for Invisible Plastic Optics. *Nano Lett.* **2019**, *19* (2), 787−792.
(30) Wang, H.; Haroldson, R.; Balachandran, B.; Zakhidov, A.; Sohal, S.; Chan, J. Y.; Zakhidov, A.; Hu, W. Nanoimprinted Perovskite Nanograting Photodetector with Improved Efficiency. *ACS Nano* **2016**, *10* (12), 10921−10928.
(31) Pourdavoud, N.; Wang, S.; Mayer, A.; Hu, T.; Chen, Y. W.; Marianovich, A.; Kowalsky, W.; Heiderhoff, R.; Scheer, H. C.; Riedl, T. Photonic Nanostructures Patterned by Thermal Nanoimprint Directly into Organo- Metal Halide Perovskites. *Adv. Mater.* **2017**, *29* (12), 7.
(32) Wei, J.; Xu, R. P.; Li, Y. Q.; Li, C.; Chen, J. D.; Zhao, X. D.; Xie, Z. Z.; Lee, C. S.; Zhang, W. J.; Tang, J. X. Enhanced Light Harvesting in Perovskite Solar Cells by a Bioinspired Nanostructured Back Electrode. *Adv. Energy Mater.* **2017**, *7* (20), 7.
(33) Mihailetchi, V. D.; Koster, L. J. A.; Blom, P. W. M. Effect of metal electrodes on the performance of polymer: fullerene bulk heterojunction solar cells. *Appl. Phys. Lett.* **2004**, *85* (6), 970−972.
(34) Gadisa, A.; Svensson, M.; Andersson, M. R.; Inganas, O. Correlation between oxidation potential and open-circuit voltage of composite solar cells based on blends of polythiophenes/fullerene derivative. *Appl. Phys. Lett.* **2004**, *84* (9), 1609−1611.
(35) He, Z. C.; Zhong, C. M.; Huang, X.; Wong, W. Y.; Wu, H. B.; Chen, L. W.; Su, S. J.; Cao, Y. Simultaneous Enhancement of Open-Circuit Voltage, Short-Circuit Current Density, and Fill Factor in Polymer Solar Cells. *Adv. Mater.* **2011**, *23* (40), 4636.
(36) Vandewal, K.; Tvingstedt, K.; Gadisa, A.; Inganas, O.; Manca, J. V. On the origin of the open-circuit voltage of polymer-fullerene solar cells. *Nat. Mater.* **2009**, *8* (11), 904−909.
(37) Qi, J.; Qiao, W. Q.; Zhou, X. K.; Yang, D. Z.; Zhang, J. D.; Ma, D. G.; Wang, Z. Y. High-Detectivity All-Polymer Photodetectors with Spectral Response from 300 to 1100 nm. *Macromol. Chem. Phys.* **2016**, *217* (15), 1683−1689.
(38) Yang, D. Z.; Zhou, X. K.; Wang, Y. P.; Vadim, A.; Alshehri, S. M.; Ahamad, T.; Ma, D. G. Deep ultraviolet-to-NIR broad spectral response organic photodetectors with large gain. *J. Mater. Chem. C* **2016**, *4* (11), 2160−2164.
(39) Wang, X.; Wang, H. Y.; Zhou, D. L.; Jin, H.; Yu, J. S. Semitransparent indium-tin-oxide-free non-fullerene organic photodetectors with double-side ultraviolet selective responses. *Mater. Lett.* **2018**, *230*, 289−292.

DOI: 10.1021/acsanm.9b01586
ACS Appl. Nano Mater. 2019, 2, 6690−6700